Sustained Solar H$_2$ Evolution from a Thiazolo[5,4-*d*]thiazole-Bridged Covalent Organic Framework and Nickel-Thiolate Cluster in Water

Bishnu P. Biswal,[†] Hugo A. Vignolo-González,[†,‡] Tanmay Banerjee,[†] Lars Grunenberg,[†,‡] Gökcen Savasci,[†,‡] Kerstin Gottschling,[†,‡] Jürgen Nuss,[†] Christian Ochsenfeld,[‡,§] and Bettina V. Lotsch*[,†,‡,§,‖]

[†]Max Planck Institute for Solid State Research, Heisenbergstraße 1, 70569 Stuttgart, Germany
[‡]Department of Chemistry, University of Munich (LMU), Butenandtstraße 5-13, 81377 München, Germany
[§]Center for Nanoscience, Schellingstraße 4, 80799 München, Germany
[‖]Nanosystems Initiative Munich (NIM), Schellingstraße 4, 80799 München, Germany

S *Supporting Information*

ABSTRACT: Solar hydrogen (H$_2$) evolution from water utilizing covalent organic frameworks (COFs) as heterogeneous photosensitizers has gathered significant momentum by virtue of the COFs' predictive structural design, long-range ordering, tunable porosity, and excellent light-harvesting ability. However, most photocatalytic systems involve rare and expensive platinum as the co-catalyst for water reduction, which appears to be the bottleneck in the development of economical and environmentally benign solar H$_2$ production systems. Herein, we report a simple, efficient, and low-cost all-in-one photocatalytic H$_2$ evolution system composed of a thiazolo[5,4-*d*]thiazole-linked COF (**TpDTz**) as the photoabsorber and an earth-abundant, noble-metal-free nickel-thiolate hexameric cluster co-catalyst assembled *in situ* in water, together with triethanolamine (TEoA) as the sacrificial electron donor. The high crystallinity, porosity, photochemical stability, and light absorption ability of the **TpDTz** COF enables excellent long-term H$_2$ production over 70 h with a maximum rate of 941 μmol h^{-1} g^{-1}, turnover number TON$_{Ni}$ > 103, and total projected TON$_{Ni}$ > 443 until complete catalyst depletion. The high H$_2$ evolution rate and TON, coupled with long-term photocatalytic operation of this hybrid system in water, surpass those of many previously known organic dyes, carbon nitride, and COF-sensitized photocatalytic H$_2$O reduction systems. Furthermore, we gather unique insights into the reaction mechanism, enabled by a specifically designed continuous-flow system for non-invasive, direct H$_2$ production rate monitoring, providing higher accuracy in quantification compared to the existing batch measurement methods. Overall, the results presented here open the door toward the rational design of robust and efficient earth-abundant COF−molecular co-catalyst hybrid systems for sustainable solar H$_2$ production in water.
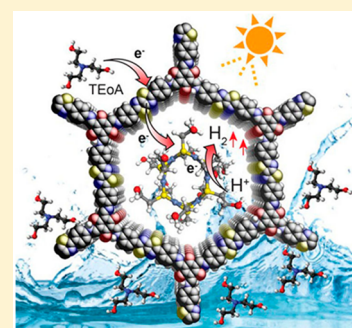
INTRODUCTION

The conversion and storage of solar energy in the form of chemical bonds in "solar fuels" like H$_2$ through light-driven water reduction has evolved into a key technology over the past decade due to the fast depletion of fossil energy sources and rapid global climate change.[1] To drive the proton reduction half reaction in an efficient way, the major challenge is to find a catalytic system that is robust and highly active, but at the same time low-cost and earth-abundant, in combination with a strongly absorbing, chemically stable photosensitizer (PS).[2] In this regard, covalent organic frameworks (COFs)[3] have recently emerged as an exciting class of photoactive materials for light-driven H$_2$ production due to their tunable light-harvesting[4] and charge-transport properties.[5] In contrast to other porous materials, COFs are known for being mechanically robust and offering large accessible surface areas. By virtue of their modular geometric and electronic structures, COFs have attracted significant interest for a range of applications including adsorption, storage and separation,[6]

chemical sensing,[7] electronics,[8] and catalysis.[9] In spite of their versatility, there are only few reports on COFs utilized as photoabsorbers for photocatalytic H$_2$ evolution so far.[10] Although it is rare and expensive, all except one of these works has employed metallic platinum as the co-catalyst to reduce water efficiently, which appears to be the bottleneck in the development of scalable, economical solar H$_2$ production. In addition, the use of nanoparticulate Pt co-catalysts precludes obtaining detailed insights into the nature of the catalytic sites and the intricacies of the photocatalytic cycle. Inspired by natural photosynthesis,[11] researchers worldwide are motivated by this shortcoming to search for single-site, earth-abundant, non-precious metal-based co-catalysts with well-defined catalytic centers. So far, only one molecular co-catalyst−COF system for photocatalytic H$_2$ evolution has been demonstrated.[12] This system is based on an azine-linked COF (N2-
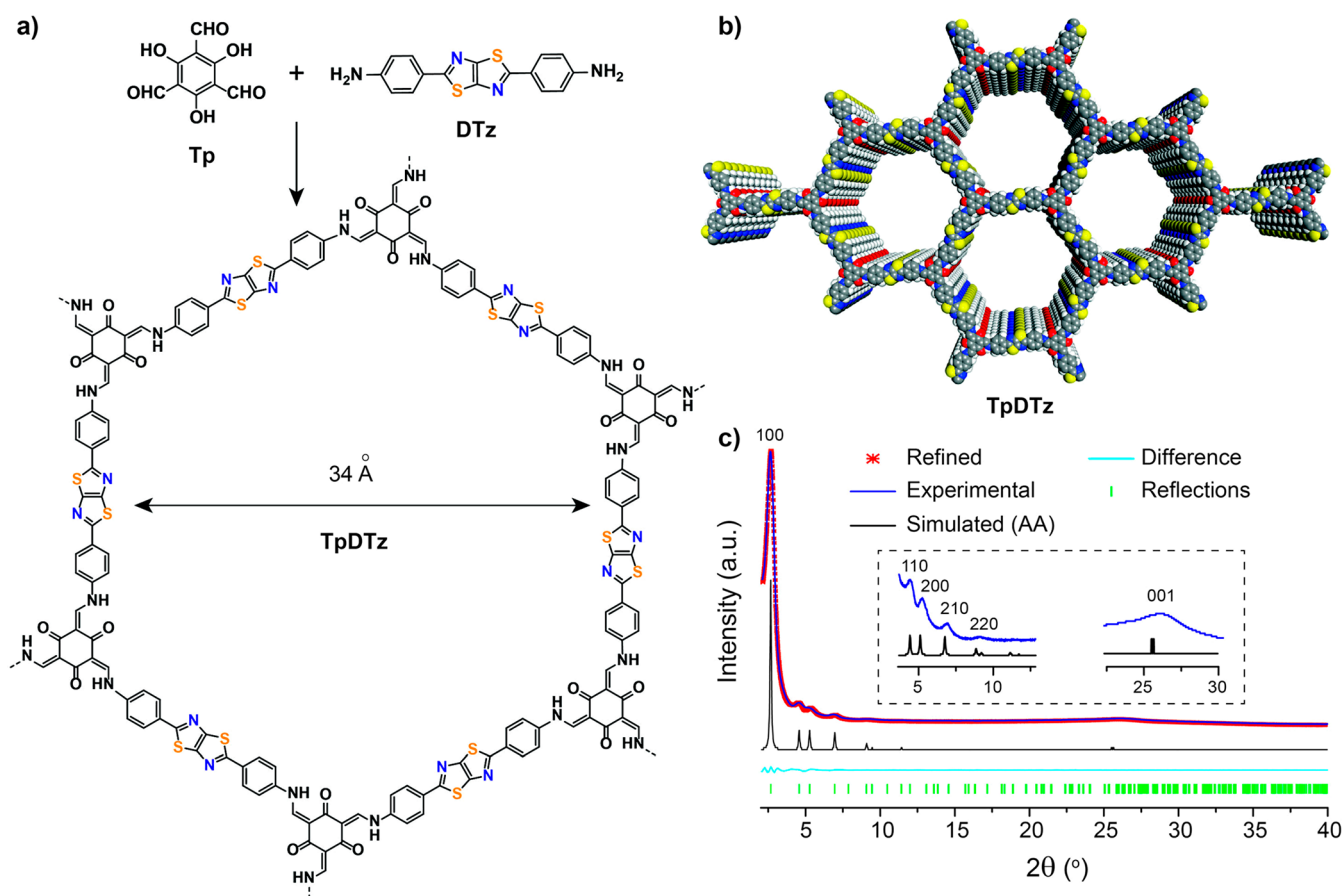
Figure 1. Synthesis and structural characterization of **TpDTz** COF. (a) Schematic representation of **TpDTz** COF synthesis. (b) Space-filling model of **TpDTz** COF pores with $\pi-\pi$ stacking of successive 2D layers (gray, C; blue, N; red, O; yellow, S; and white, H). (c) Indexed PXRD patterns of **TpDTz** COF with corresponding Pawley refinement (red) showing good fit to the experimental data (blue) with minimal differences (cyan); the inset shows close-up of the indexed experimental (blue) and simulated (black) PXRD patterns based on Pawley fits [final R_{wp} = 2.59% and R_p = 1.89%].

COF)[10b] acting as the PS and a cobaloxime molecular proton reduction catalyst, which shows a H_2 evolution rate of 782 μmol h^{-1} g^{-1} and a turnover number TON$_{Co}$ = 54.4. However, the limited photostability and especially the utilization of an organic solvent (acetonitrile/water mixture; 4:1) were major concerns.[12]

Notably, a majority of molecular catalysts decompose during prolonged catalysis, are inherently insoluble in water, and require the addition of organic solvents to accomplish water reduction.[13] With cobaloxime-based systems, for example, the catalyst often converts to an inactive form within a few hours (<6 h) of H_2 evolution, possibly due to ligand decomposition or hydrogenation.[14]

To overcome these issues, the development of a scalable, earth-abundant, and low-cost co-catalyst system which is soluble in water and can be coupled efficiently to a molecularly defined heterogeneous photoabsorber is in high demand. In this regard, Ni-based synthetic photocatalytic H_2 evolution catalysts[15] have attracted significant interest because of their robust and oxygen-tolerant nature and, importantly, their structural similarity to the active site in [Ni-Fe] hydrogenase.[16]

Likewise, small molecules and polymers containing fused (bi)heterocyclic thiazolo[5,4-d]thiazole (TzTz) moieties have received much attention as semiconductors in organic electronics lately because of their n-type character featuring high oxidative stability and their rigid planar structure.[17a] The

latter enables efficient intermolecular $\pi-\pi$ overlap that affords high electron and hole mobility.[17] Such TzTz moieties further feature excellent photoabsorbing ability, which is likewise beneficial for photocatalysis.[2a] Nevertheless, TzTz-based COFs have not been explored so far. Notably, thus far, only a very limited number of COFs bearing photoactive functionalities such as triazine,[10a,b] diacetylene,[10c] or sulfone moieties[10d] have been shown to produce H_2 from water, with the noble metal Pt acting as co-catalyst.

Combining these aforementioned leverages, in this work, we present a light-driven hybrid proton reduction system employing a newly designed TzTz-linked COF (**TpDTz**) as a photoabsorber and a molecular Ni-thiolate cluster (NiME)[18] assembled *in situ* from a Ni(II) salt and 2-mercaptoethanol (ME). The combination of the NiME cluster co-catalyst and **TpDTz** COF enables sustained H_2 evolution with an excellent rate (941 μmol h^{-1} g^{-1}) and a TON$_{Ni}$ > 103 (70 h) in the presence of triethanolamine (TEoA) as the sacrificial electron donor (SED) in water under AM 1.5 light illumination. We thus report a single-site heterogeneous COF-based photocatalyst system that operates with a noble-metal-free co-catalyst in *water* as the solvent. We further carve out structure−property−activity relationships by comprehensively screening the parameter space of this heterogeneous−homogeneous hybrid photocatalytic system, including pH, SED, co-catalyst metal centers, different N/S-containing chelating ligands for
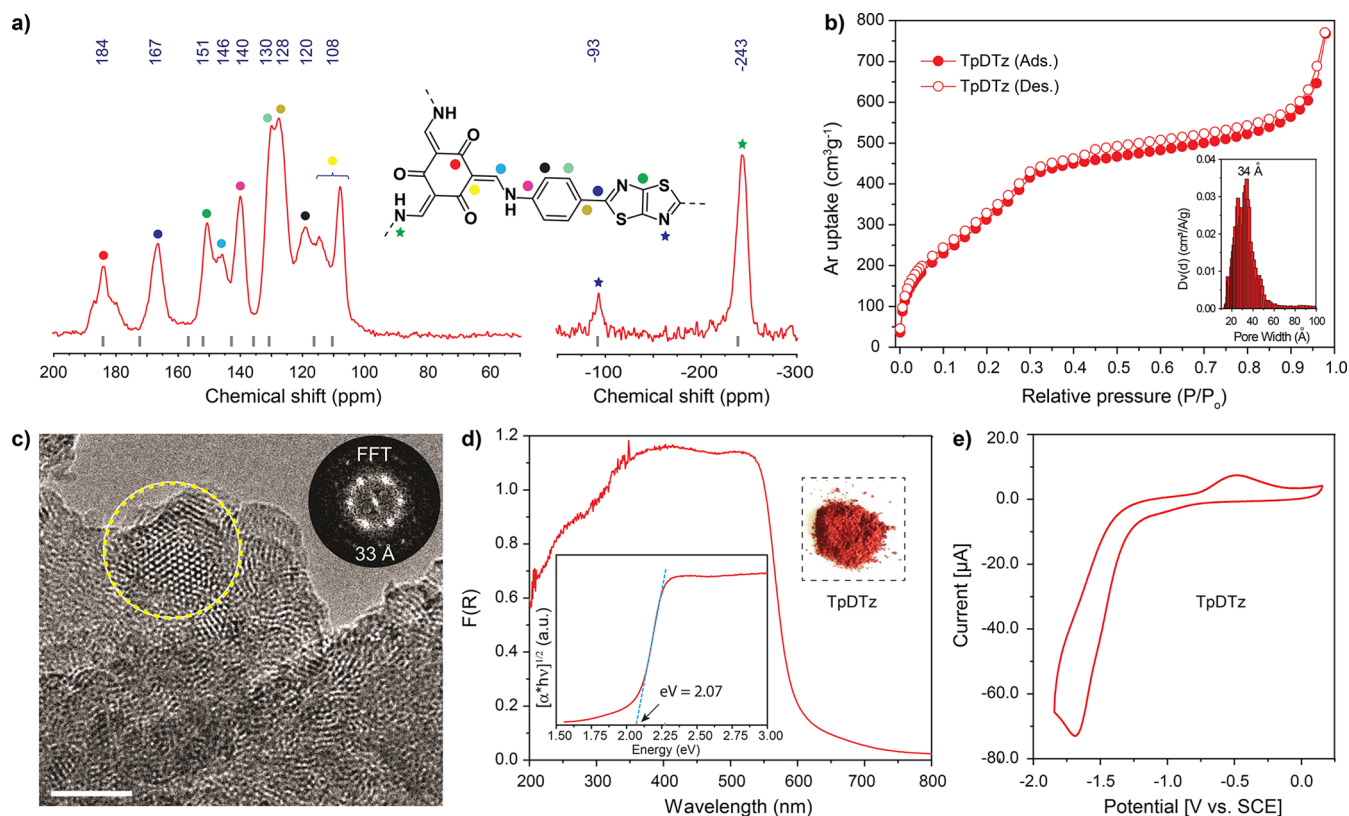
Figure 2. Structural characterization of **TpDTz** COF. (a)^{13}C and ^{15}N CP-MAS solid-state NMR spectra of **TpDTz** COF. Calculated NMR chemical shifts for the **TpDTz**-NMR model (Figure S49) obtained at the B97-2/pcS-2//PBE0-D3/def2-TZVP level of theory (Tables S4 and S5) are shown as gray dashes. (b) Argon adsorption−desorption isotherm for **TpDTz** COF recorded at 87 K; inset shows calculated pore size distribution of **TpDTz** COF according to the QSDFT method. (c) TEM image of **TpDTz** COF showing the hexagonal pore structure with a periodicity of ∼3.3 nm (scale bar, 100 nm). (d) UV−vis diffuse reflectance (DR) spectrum for **TpDTz** COF measured in the solid state; insets show a plot of the Kubelka−Munk function to extract the direct optical band gap and a photograph of **TpDTz** COF powder. (e) Cyclic voltammogram (CV) of a **TpDTz** COF-modified FTO working electrode in 0.1 M NBu$_4$PF$_6$ as the supporting electrolyte in anhydrous acetonitrile at a scan rate of 100 mV/s.

co-catalysts, and a variety of PSs. Also, our study is built on a continuous-flow photocatalytic reactor system which enables a non-invasive and direct monitoring of the H$_2$ evolution rate with high accuracy, in contrast to the routinely used standard photocatalytic batch reactors, and this allows gathering unique insights into the photocatalytic reaction modeling and kinetics. The results and understanding presented here thus contribute toward the rational development of robust and efficient single-site hybrid photocatalytic systems as a sustainable solution for solar H$_2$ production in water.

■ RESULTS AND DISCUSSION

COF Synthesis and Characterization. The precursor 4,4′-(thiazolo[5,4-d]thiazole-2,5-diyl)dianiline (**DTz**) was synthesized as described in the Supporting Information and characterized using single-crystal X-ray diffraction, nuclear magnetic resonance (NMR) spectroscopy, Fourier transform infrared (FTIR) spectroscopy, and mass spectrometry. **TpDTz** COF was synthesized by solvothermally reacting 1,3,5−triformylphloroglucinol; **Tp** (1.0 equiv) and **DTz** (1.5 equiv) in the presence of 6 M aqueous acetic acid using an o-dichlorobenzene and N,N-dimethylacetamide solvent combination in a high-precision glass vial, which was sealed and heated to 120 °C for 3 days (Figure 1 and Supporting Information section S2). Following a similar protocol, **TpDTP**

COF with a similar pore size was synthesized as a reference,[19] with the **DTz** linker replaced with the linear terphenyl linker.

To verify crystallinity and phase purity, the as-synthesized **TpDTz** COF was analyzed via powder X-ray diffraction (PXRD). The PXRD pattern exhibits an intense first peak at 2.56° 2θ corresponding to the 100 reflection along with other diffraction peaks at 4.41, 5.23, 6.90, and 9.10° 2θ, attributed to the 110, 200, 210, and 220 reflections, respectively. In addition, at ∼26° 2θ a broad set of reflections is visible, with 00l being the most intense, which corresponds to the π−π stacking of the 2D layers (Figure 1c). The experimental PXRD pattern is in good agreement with the simulated AA eclipsed stacking model (Figure S6.2). The lattice parameters of **TpDTz** COF were extracted by Pawley refinement in the hexagonal space group P6/m (a = b = 39.27 Å, c = 3.46 Å, α = β = 90°, and γ = 120°) (Figure 1c). The relatively high level of order observed with PXRD may originate from effective π−π stacking interactions facilitated by the planarity of the **DTz** linker and, thus, the 2D layers. The measured pore aperture is ∼3.4 nm, and the π−π stacking distance between individual layers is ∼3.5 Å for **TpDTz** COF, as obtained from the structural model.

The FTIR spectrum of the as-synthesized **TpDTz** COF shows bands at ∼1254 cm^{-1} (−C−N), ∼1571 cm^{-1} (C=C), and ∼1618 cm^{-1} (C=O) (Figure S9), which confirms the formation of the proposed β-ketoenamine-linked framework.

The TzTz moiety was identified by appearance of C=N vibrations (~1660 cm^{-1}) and C–S stretching bands between 650 and 700 cm^{-1}. The structural composition of **TpDTz** COF was further confirmed by ^{13}C cross-polarization magic-angle spinning (CP-MAS) NMR spectroscopy (Figure 2a). The spectrum shows signals corresponding to the heterocyclic TzTz ring of the **DTz** building unit ($\delta \approx 151$ ppm), together with a characteristic signal of the carbonyl carbon (C=O) at ~184 ppm, which further supports formation of the β-ketoenamine moiety. ^{15}N NMR spectroscopy confirms the presence of two different kinds of nitrogen atoms with chemical shifts of −93 and −243 ppm, corresponding to the TzTz and enamine (=C–NH–) moieties, respectively (Figure 2a). All assignments are supported by quantum-chemical calculations of NMR chemical shifts (Tables S4 and S5) at the B97-2/pcS-2//PBE0-D3/def2-TZVP level using the FermiONs++ program package[20a,b] based on a selected molecular model system (Figure S49). The corresponding structures were optimized at the PBE0-D3/def2-TZVP level using Turbomole (version 7.0.3).[20c,d] Scanning electron microscopy (SEM) images of **TpDTz** COF reveal a flower-like morphology composed of flakes with 1−3 μm lateral dimensions (Figure S11). Transmission electron microscopy (TEM) images confirm the layered morphology of the crystalline network with clearly visible 2D honeycomb-type pores oriented perpendicular to the crystallographic c axis with a periodicity of ~3.3 nm (Figure 2c). In order to evaluate the thermal stability of **TpDTz** COF, we further performed thermogravimetric analysis (TGA) in air. The TGA profile suggests that the COF pores are guest free and the material is thermally stable up to ~400 °C (Figure S10).

The permanent porosity of **TpDTz** COF was assessed by Ar adsorption analysis measured at 87 K (Figure 2b and Figure S13). A Brunauer−Emmett−Teller (BET) surface area of 1356 m^2 g^{-1} was obtained for **TpDTz** COF, which is comparable to some of the most porous β-ketoenamine-based porous COFs previously synthesized via solvothermal methods.[10c,d,21] The experimental pore size of 3.4 nm obtained from the adsorption isotherm using the quenched solid state density functional theory (QSDFT) cylindrical-slit adsorption kernel for carbon (inset of Figure 2b) is in excellent agreement with the pore size obtained from the structure model (~3.4 nm) and TEM (~3.3 nm). Further, the measured water adsorption isotherm (total uptake 309 cm^3 g^{-1}, 25 wt% at STP) of **TpDTz** COF suggests its relatively hydrophilic nature, induced by the polar N/S containing TzTz group and should thus lead to higher dispersibility of the COF in water during photocatalysis,[10d,e] as opposed to the non-TzTz **TpDTP** COF (total uptake 75 cm^3 g^{-1}, 6 wt% at STP) with similar pore sizes (Figure S15). This fact is also supported by the higher CO_2 uptake for **TpDTz** COF compared to **TpDTP** COF (Figure S16).

Since chemical stability is a crucial criterion for any material to be considered for practical applications, we investigated the chemical stability of **TpDTz** COF under strongly acidic (12 M HCl) conditions and in boiling water up to 7 days. The retention of all characteristic peaks in the PXRD pattern suggests a high chemical stability under the tested conditions (Figure S7). It is important to note that **TpDTz** COF is stable only under mild basic conditions (1 M KOH) for up to 3 days, while at harsher basic conditions (12 M KOH for 7 days) the framework decomposes. The high chemical tolerance of **TpDTz** COF is ascribed to the combined effect of the stabilizing enol-to-keto tautomerism[21] and the planarity of the

TzTz moiety,[17] which allows for strong $\pi-\pi$ interactions between the layers.

Optoelectronic Properties and Photocatalysis. The UV−vis diffuse reflectance (DR) spectrum of **TpDTz** COF reveals efficient light absorption extending into the orange parts of the visible spectrum with an absorption edge at ~598 nm (Figure 2d). Kubelka−Munk analysis yields a direct optical band gap of ~2.07 eV. In contrast, **TpDTP** COF shows a blue-shifted absorption band edge at ~531 nm, corresponding to a larger optical band gap of ~2.28 eV (Figure S18), due to the absence of light harvesting TzTz units. The measured photoluminescence (PL) spectra (Figure S19) reflect this trend; **TpDTz** COF has a significantly red-shifted emission (λ_{max} = 690 nm) compared to **TpDTP** COF (λ_{max} = 630 nm). The fluorescence decays can be fitted with triexponential functions, and the amplitude-weighted average lifetimes for **TpDTz** and **TpDTP** COFs are 94 and 115 ps, respectively (Figure S20). Emission intensities were too low to measure accurate absolute emission quantum yields. The short excited-state lifetimes together with low emission quantum yields suggest more pronounced non-radiative rates in the COF systems, relative to the radiative rates, similar to our previously reported N3-COF system.[10b,f]

Cyclic voltammograms (CV) of **TpDTz** COF films were measured to estimate the band positions and the thermodynamic driving force for H_2 evolution. The voltammogram of a **TpDTz** COF-modified FTO working electrode[22] shows an irreversible reduction wave with an onset potential of $E_{red,onset} \approx -1.24$ V vs saturated calomel electrode (SCE) (Figure 2e and Figure S22). From the optical bandgap (E_g = 2.07 eV) determined from the UV−vis DR spectrum, the valence band (VB) and conduction band (CB) edges of **TpDTz** COF can be estimated to be $E_{CB} = -3.46$ eV and $E_{VB} = -5.53$ eV vs the vacuum level, following the equations $E_{CB} = -(E_{red,onset \, vs \, SCE} + 4.7)$ eV and $E_{VB} = E_{CB} - E_{g,opt}$.[23] Quantum-chemical calculations of vertical ionization potentials and electron affinities on a **TpDTz** pore model (Figure S53), cut from a supercell built using the 2D periodic optimized unit cell of the **TpDTz** COF (Figure S52), support these findings (Table S8). Based on a comparison of these values with the oxidation potential of TEoA (0.57 V vs SCE)[23d] and the reduction onset potential of the NiME molecular catalyst system (−0.75 V vs SCE) (Figure S21), it is likely that **TpDTz** COF can transfer electrons to the NiME co-catalyst system, forming a reduced Ni(I) center and thereby enabling H_2 evolution in successive steps.[18,23a] Also, TEoA can efficiently quench the photoexcited holes in the COF thereby replenishing its photoactivity.

Owing to the planar and conjugated structure, the electron-deficient nature of the heterocyclic backbone, and the optimal band gap and hence light absorption ability, the TzTz-linked **TpDTz** COF was investigated as the heterogeneous photo-absorber for photocatalytic H_2 evolution in combination with the Ni-thiolate hexameric cluster (NiME) co-catalyst in water. The NiME cluster co-catalyst has a cyclic hexameric structure composed of six Ni(II) ions forming a planar ring, and the Ni centers are bridged by 12 ME units, which has been confirmed by DFT calculation and single-crystal X-ray diffraction analysis by others (Figure S35).[18,24b] This NiME cluster co-catalyst has been shown to produce H_2 actively when sensitized by an organic xanthene dye (erythrosin B).[18] However, the generation of unstable PS radical species upon photochemical quenching of the excited-state dye (PS*) leads to a fast decomposition and hence poor photochemical stability of
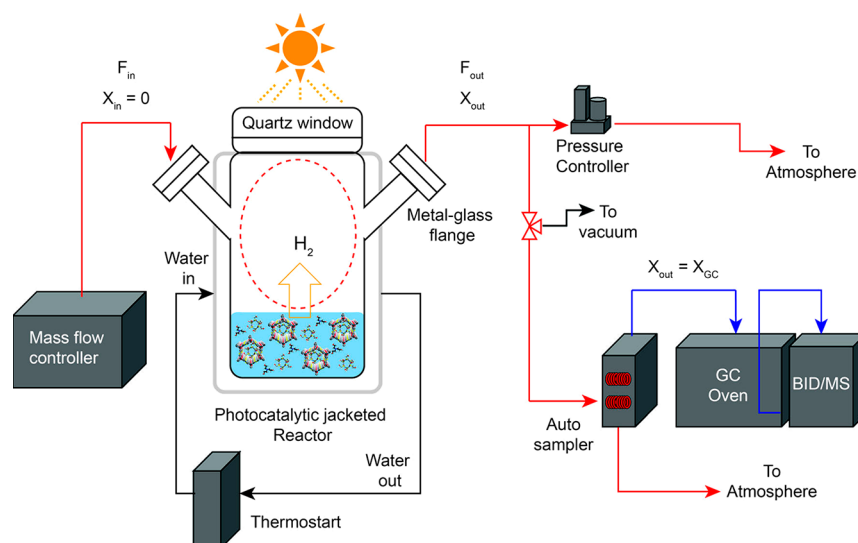
Figure 3. Continuous-flow photocatalytic reactor design. Schematic diagram of the designed continuous-flow photocatalytic reactor system (red streamlines are the continuous-flow pathway of gas). In contrast, the batch configuration involves mass flow controllers as dead-ends after back purging the initial headspace and replaces the autosampler by a septa-port or a manual sampling valve.

organic dye PSs, which hinders the long-term performance of the photocatalytic system.[15a,18] The strategy of combining a photochemically stable COF photoabsorber with the Ni-thiolate cluster co-catalyst in water could thus be a viable path to impart better long-term stability for H_2 production.

The beauty of the aforesaid NiME complex lies in its simple, quick *in situ* synthesis in water upon addition of a Ni(II) salt and ME at room temperature. This *in situ* assembly strategy is different from those of most other Ni(II) and Co(II) co-catalyst complexes, featuring arduous *ex situ* synthesis and purification of a water-soluble analogue, thus adding to the cost-effectiveness of the NiME cluster co-catalyst approach.[12,15]

In addition, this cluster has been shown to be a potent H_2 evolution co-catalyst producing H_2 immediately after light illumination in the presence of a PS and SED, and hence does not require any photodeposition, nor does it show an activation time, contrary to Pt-based photocatalytic systems.[10]

For better measurement accuracy and to gain insights into the photocatalytic mechanism, we developed a continuous-flow system to monitor the H_2 evolution performance of the hybrid photocatalytic system (Figure 3 and Figure S23). In this measurement system, the molar flow entering the system, the pressure (0.5 bar), and the temperature (25 °C) of the reactor are continuously controlled, while bypassing some of the outflow to an open sampling loop gas chromatograph (GC) autosampler. In this way, the rate of H_2 production (R_{H_2}) can be monitored directly using only two experimental inputs: F_{in} from the mass flow controller, and $x_{H_2,ppm}$ from an online GC (BID) detection system (eq 1), where F_{in} is the carrier gas (in this case He) flow in to the system and $x_{H_2,ppm}$ is the molar fraction of H_2 at the outlet.

$$R_{H_2} = \frac{F_{in} \times x_{H_2,ppm} \times 10^{-6}}{(1 - x_{H_2,ppm} \times 10^{-6})} \quad (1)$$

Typically, the run-to-run error with this method is below 3%, compared to at least 15−20% error with a standard batch system. Also, this continuous-flow system is independent of

experimental conditions and does not require human intervention when sampling or local derivative approximations as with regular batch system measurements (Figure S34). In addition to the better accuracy of this method in monitoring kinetic trends in the photocatalytic H_2 evolution process, the method also keeps the media unperturbed—since the presence of the GC sampling line does not affect the hydrogen balance—thus completely eliminating typical sampling losses and mathematical and experimental uncertainties associated with batch photocatalytic reactor systems.

In a typical photocatalytic experiment using our hybrid system, 5 mg of **TpDTz** COF was dispersed in 10 mL of H_2O containing TEoA (10 vol%) as the SED, and the pH was adjusted to 8.5 by adding HCl. Ni(OAc)$_2$·4H$_2$O (10 wt%, 0.5 mg) and ME (10 equiv, 1.4 μL) were then charged to instantaneously form the brown-colored NiME cluster co-catalyst. When irradiated with 100 mW/cm^2 AM 1.5 radiation, the resulting mixture produces H_2 actively over a period of at least 70 h—with ~40% of the highest production rate still preserved after this time—in a single run without adding additional TEoA or co-catalyst (Figure 4a). A maximum H_2 evolution rate of 941 μmol g^{-1} h^{-1} with a TON$_{Ni}$ > 103 (70 h) and a TOF = 2.3 h^{-1} when the system is fully active were obtained. A mathematically projected (Supporting Information section S8) TON$_{Ni}$ > 443 (890 μmol of total H_2 evolution) can be obtained for the photocatalytic H_2 evolution performance corresponding to a complete depletion of the co-catalyst. The relation between co-catalyst, SED, and observed activity loss of the system in time was confirmed by *in situ* addition of loss-equivalent amounts of ME or TEoA independently after 72 h of illumination, which did not change the deactivation trends observed (Supporting Information, section S8). It must be noted that the TON$_{Ni}$ mentioned above is only a lower limit calculated based on the total amount of Ni(II) salt used for the photocatalysis experiment. Under identical conditions the erythrosin B (EB) dye-sensitized system[18] produces H_2 with a maximum rate of 49 297 μmol g^{-1} h^{-1} (attained in 1 h); however, the rate rapidly drops off, and the whole system becomes completely inactive within 7 h. A TON$_{Ni}$ > 36.5 (73 μmol of total H_2 evolution) was obtained after 7 h (TOF$_{Ni}$ =
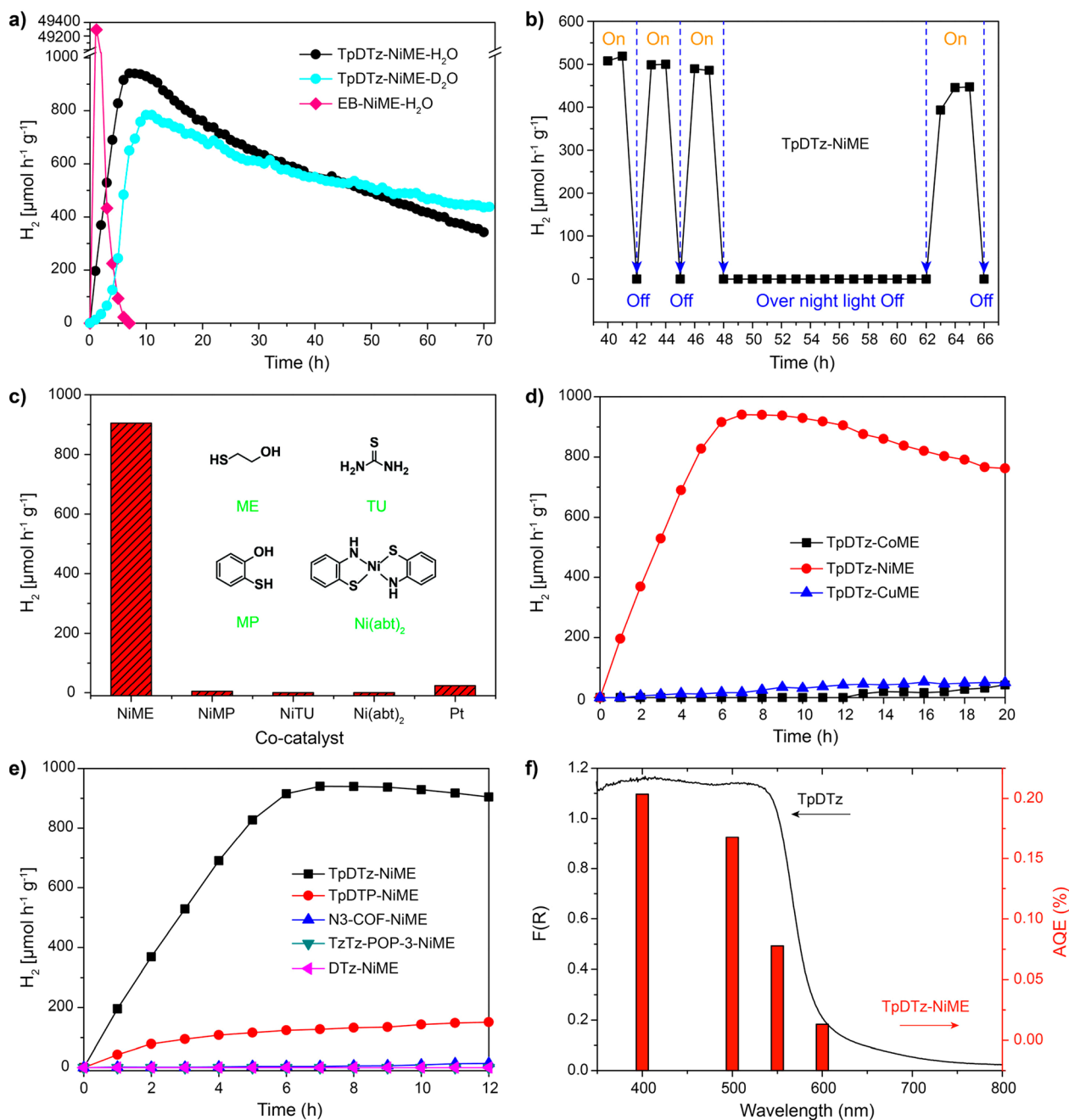
Figure 4. Photocatalytic H_2 evolution. (a) Comparison of photocatalytic H_2 evolution rates in water (H_2O) and deuterium oxide (D_2O), using **TpDTz** COF over 72 h and **EB** dye under AM 1.5 light irradiation [COF photosensitizer: 5 mg of **TpDTz** COF in 10 mL of H_2O/D_2O with 10 vol % TEoA, 0.5 mg of $Ni(OAc)_2$, and 1.4 μL of ME at a final pH of 8.5; dye photosensitizer: 1.33 mg of **EB** in 10 mL of H_2O with 10 vol% TEoA, 0.5 mg of $Ni(OAc)_2$, and 1.4 μL of ME at a final pH of 8.5]. (b) Light *on−off* cycles for photocatalytic H_2 evolution experiments with **TpDTz** COF in water over 26 h. (c) Photocatalytic H_2 evolution with **TpDTz** COF in water using different co-catalysts. (d) Photocatalytic H_2 evolution with **TpDTz** COF in water using different metal-ME co-catalysts. (e) Photocatalytic H_2 evolution from water using different photosensitizers. (f) Overlay of the UV−vis DR spectra of **TpDTz** COF with apparent quantum efficiency (AQEs) for the photocatalytic H_2 evolution reaction with **TpDTz** COF at four different incident light wavelengths.

31.9 h^{-1}), which is 12 times lower than the value projected for the **TpDTz** COF-sensitized system (Figure 4a). These results demonstrate the added value of using a heterogeneous PS to stabilize charge transfer in photocatalytic hybrid systems.

Also, the **TpDTz** COF-NiME photocatalytic system produces H_2 at a 17% higher maximum rate and has a TON nearly 8-fold as high as our previously reported N2-COF-cobaloxime-based system (782 $\mu mol\ h^{-1}\ g^{-1}$, $TON_{Co} = 54.4$), while operating in water.[12] The H_2 evolution rate and the

sustained activity of this simple **TpDTz** COF-NiME system are competitive with and even superior to those of many COF-based photocatalytic systems (Table S3) and other benchmark photocatalytic systems involving metallic Pt or molecular Ni co-catalysts. Examples include g-C_3N_4/Pt (840 $\mu mol\ g^{-1}$ h^{-1}),[25b] TP-BDDA/Pt (324 $\mu mol\ g^{-1}\ h^{-1}$),[10c] N2-COF/Pt (480 $\mu mol\ g^{-1}\ h^{-1}$),[10b] crystalline poly(triazine imide)/Pt (864 $\mu mol\ g^{-1}\ h^{-1}$),[25a] sg-CN-Ni (103 $\mu mol\ g^{-1}\ h^{-1}$),[25c] $Ni_{12}P_5$/g-C_3N_4(536 $\mu mol\ g^{-1}\ h^{-1}$),[25d] $^{NCN}CN_x$-NiP (763 μmol

g^{-1} h^{-1}),[25e] and carbon quantum dots (CQDs)-Ni (398 μmol g^{-1} h^{-1}).[25f]

Control experiments were performed by sequentially removing one of the components, i.e., **TpDTz** COF, TEoA, Ni(OAc)$_2$·4H$_2$O, and ME, at a time from our photocatalytic system to identify their importance and role for the H$_2$ evolution. Indeed, no H$_2$ evolution was observed for a period of 12 h unless all individual components act in concert, signifying that each is essential for the photocatalytic system to work and efficiently produce H$_2$ (Figure S27).

Furthermore, a 1:10 metal-to-ligand molar ratio and 10 wt% of catalyst with respect to the PS were observed to elicit the best photocatalytic performance (Figures S28 and S29). To confirm water as the source of H$_2$, the photocatalytic reaction was performed in D$_2$O under identical conditions (Figure 4a). A production rate for D$_2$ in D$_2$O similar to that for H$_2$ in H$_2$O was observed over 72 h, taking batch-to-batch variations into account. This result suggests that water is the hydrogen source responsible for the production of H$_2$, assuming that no significant proton/deuterium exchange processes in the individual components are at play. This finding was further confirmed by an almost complete disappearance of the $m/z = 2$ signal for H$_2$ in a mass spectrometric measurement of the headspace gas of the photocatalytic reaction performed in D$_2$O (Figure S26). Note that D$_2$ is evolved with a time lag compared to H$_2$, which is likely due to the kinetic isotope effect (KIE) of deuterium as described below. Further, H$_2$ evolution experiments performed under multiple light *on−off* cycles over a period of 26 h (Figure 4b) suggests a purely light driven H$_2$ evolution process in water. Once the catalytic system is fully active, H$_2$ evolution activity is seen to be restored even after a prolonged light *off* period.

SED and the reaction pH are known to have a profound influence on the activity of many H$_2$ production systems.[10b,c,12] In our case, we observed a similar effect; the rate of H$_2$ generated from the photochemical reaction is the highest (941 μmol g^{-1} h^{-1}) at pH 8.5 using TEoA as SED. However, at acidic conditions (pH 6.5) there was negligible H$_2$ evolution (16 μmol g^{-1} h^{-1}). This could be attributed to the protonation of TEoA or due to inhibition of proton loss from one-electron oxidized TEoA$^+$.[13c] Notable H$_2$ evolution is observed over 24 h under alkaline conditions (pH 11), albeit at lower rates (308 μmol g^{-1} h^{-1}) as compared to pH 8.5 (Figure S30). This is possibly due to the reduced driving force for protonation of the Ni hydride intermediate co-catalyst species at higher pH to subsequently generate H$_2$. Triethylamine (TEA) and Na$_2$S were also explored as potential SEDs. Interestingly, they produce H$_2$ but with significantly lower rates of 84 μmol g^{-1} h^{-1} and 7 μmol g^{-1} h^{-1}, respectively (Figure S31). Higher TEoA concentrations were found to decrease H$_2$ evolution rates; a TEoA concentration of 10 vol% in water was observed to result in the maximum H$_2$ production rate (Figure S32).

H$_2$ evolution rates of the photocatalytic systems containing **TpDTz** COF PS and different Ni(II)co-catalysts were measured (Figure 4c). Different sulfur-containing compounds, such as thiourea (TU) and 2-mercaptophenol (MP), were explored as potential ligands for *in situ* formation of Ni(II)co-catalyst complexes. However, neither NiTU nor NiMP produced any H$_2$ with **TpDTz** COF, possibly due to unfavorable complexation of the ligands with Ni(II) in water: TU and MP are known to be poorer complexation agents as compared to ME.[26] Also, a reported *ex situ* synthesized Ni(abt)$_2$ complex[15c] was studied as a potential

H$_2$ evolution co-catalyst under our experimental conditions, but no H$_2$ evolution was seen, most likely due to its poor solubility in water. It is also interesting to note that **TpDTz** COF produces H$_2$ with a significantly smaller rate of 23 μmol g^{-1} h^{-1} with metallic Pt co-catalyst and TEoA at pH 8.5 over a period of 24 h as compared to that with NiME. The significant difference between H$_2$ evolution of the molecular co-catalyst and photodeposited Pt nanoparticles is difficult to explain by a single effect.[12,25f] However, it may be argued that the higher activity of the NiME co-catalyzed system in contrast to the surface bound Pt nanoparticles (Figure S48) is due to a more effective blocking of charge carrier recombination since the co-catalyst is physically separated from the framework (physisorbed), which may support better charge separation. We further screened the H$_2$ evolution activity of other transition metal-ME complexes, such as CoME and CuME, with **TpDTz** COF as the PS following a similar method as that of NiME. Although all systems produced H$_2$, they do so with a much lower rate following the order NiME (941 μmol g^{-1} h^{-1}) > CoME (85 μmol g^{-1} h^{-1}) > CuME (52 μmol g^{-1} h^{-1}). This could be due to the poor solubility of CoME and CuME clusters in water compared to the NiME, which is in accordance with the reported dye sensitized molecular system[18] (Figure 4d).

We then evaluated the H$_2$ evolution ability of the NiME cluster co-catalyst with a variety of photoabsorbing materials; **TpDTP** COF,[19] N3-COF,[10b] an amorphous porous polymer containing TzTz groups (TzTz-POP-3),[27] and the diamine linker **DTz** were tested under identical conditions. Even though N3-COF is considered one of the most active COFs for photocatalytic H$_2$ generation (reported rate of 1700 μmol g^{-1} h^{-1} when co-catalyzed by Pt),[10b] with NiME co-catalyst it produces H$_2$ only at a very low rate of 40 μmol g^{-1} h^{-1} (Figure 4e). Under similar conditions **TpDTP** COF produces H$_2$ at a rate of 160 μmol g^{-1} h^{-1}, which is nearly 6 times less compared to that of the **TpDTz** COF sensitized system. The marked difference in photocatalytic activity between **TpDTz** COF and **TpDTP** COF may in part be rationalized by the reaction conditions which were not optimized specifically for **TpDTP** COF, but also by their different photon absorption characteristics. A redshift of ∼67 nm is observed for **TpDTz** COF with respect to **TpDTP** COF, which indicates that **TpDTz** COF absorbs photons more effectively in the visible range. This said, increased reactivity is only expected if the conduction band is not significantly lowered to maintain the thermodynamic driving force for the HER. In addition to that, the higher crystallinity and the higher BET surface area of 1356 m^2 g^{-1} for **TpDTz** COF versus 736 m^2 g^{-1} for **TpDTP** COF, along with a better dispersibility of the more hydrophilic **TpDTz** COF in aqueous solution, are likely determining factors for the enhanced photocatalytic activity. Notably, the amorphous polymer TzTz-POP-3 and the diamine linker **DTz** are completely inactive at producing H$_2$ with the NiME co-catalyst (Figure 4e). Overall, the significantly lower reactivity of other PSs in producing H$_2$ with the NiME co-catalyst is rationalized by a combined effect of unfavorable charge-transfer processes, reduced light harvesting, low crystallinity and surface area, and poor dispersibility in water.

The apparent quantum efficiency (AQE) was calculated using four different bandpass filters with central wavelengths (±20 nm) at 400, 500, 550, and 600 nm to quantify the spectral contribution toward H$_2$ evolution activity of the **TpDTz** COF photoabsorber. Figure 4f shows that **TpDTz**
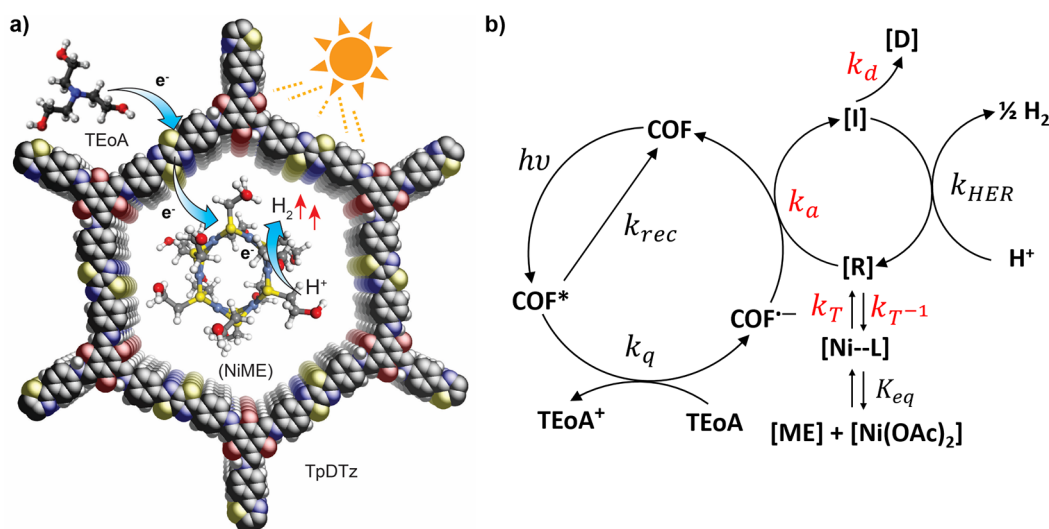
Figure 5. Reaction limitations insights. (a) General schematic of the proposed pathway for H$_2$ evolution (color code: gray, C; red, O; yellow, S; blue, N; and light pink/white, H). (b) Proposed key steps of the photocatalytic H$_2$ evolution reaction with **TpDTz** COF and NiME cluster co-catalyst. [Ni-L] denotes a ligand-coordinated co-catalyst state which is attained fast compared to the [R] state, [R] denotes the catalyst resting state, which is catalytically active nickel cluster species, [D] denotes the deactivated species, and [I] denotes an intermediate reduced catalyst species able to run the HER step.

COF has a maximum AQE of 0.2% at 400 nm. Under AM 1.5 illumination, the AQE was estimated to be 0.044%, which is higher than that of our previously reported N2-COF-cobaloxime H$_2$ evolution system (0.027%).[12]

We further verified the photochemical stability of **TpDTz** COF after a 72 h long photocatalysis experiment. The isolated **TpDTz** COF sample was fully characterized using PXRD, ssNMR, SEM, and TEM, and it was found that the framework structure, crystallinity, and morphology of **TpDTz** COF are retained (Supporting Information, section S9), thus supporting the high chemical stability of this COF (*vide supra*). A small additional signal at 56.6 ppm in the ^{13}C ssNMR spectrum possibly corresponds to trapped ME molecules inside the **TpDTz** COF pore. This, together with the observation of traces of Ni in the post-photocatalytic **TpDTz** COF using SEM-EDAX (Figure S46) may hint to chemisorption of small amounts of co-catalyst to the COF walls. However, ^{15}N ssNMR of the **TpDTz** COF sample does not show any noteworthy difference in the chemical shifts of the N signals before and after photocatalysis (Figure S41), suggesting that there is no substantial direct interaction between the residual Ni and the nitrogen centers of the COF. Also, the as-recovered **TpDTz** COF sample does not produce any H$_2$ under identical photocatalytic conditions except for the absence of Ni(OAc)$_2$· 4H$_2$O and 2-ME ligand. This suggests that the interaction between **TpDTz** COF and NiME is mostly physical, and no lasting chemical interaction exists between the two components. Our finding thus suggests an outer-sphere electron transfer to be at play, which nevertheless is efficient enough to allow facile charge transfer from the photoabsorber to the NiME co-catalyst (Figure 5a).

To obtain deeper insights into the photocatalytic mechanism, an overall coarse-grain mathematical model (Supporting Information eq S6.2) of the photocatalytic reaction was developed (see Supporting Information section S8 for details) by taking advantage of the quantification of hydrogen evolution rates in our flow detection platform. Our model was based on three primary experimentally observed trends: the activation time required by the photocatalytic system to

reach maximum rates in the first run (Figure 4a), the absence of this activation time during light *on−off* cycles or long dark periods before illumination (Figure 4b), and the KIE in D$_2$O, namely, smaller deuterium evolution rates and delayed response, together with the observation of a similar initial activation time as with H$_2$O (Figure 4a). A possible reaction model is outlined in Figure 5b. The absence of an activation time during light *on−off* cycles (Figure 4b) suggests a light enhanced formation of a catalyst resting state [R] of the NiME complex upon illumination, as seen by the initial activation time required for the system to reach maximum efficiency. The reaction network can then be reduced to the following core steps using a microkinetics analysis. For the heterogeneous (COF) fast cycle: COF photoexcitation ($h\nu$), exciton recombination in the COF (k_{rec}), reductive quenching of the COF (k_q), and electron transfer from COF$^{\bullet-}$ to [R] to form the active intermediate species [I] (k_a). Quantum-chemical calculations on the **TpDTz** pore model system (Figure S55) identify the lowest photoexcitation energy to be 2.30 eV (Table S9), the difference density of this excited state (Figure S57) visualizing the exciton. The spin density of the radical anion as a result of the reductive quenching of this state is shown in Figure S58. For the homogeneous (catalyst) cycle: formation of a rapidly coordinated complex [Ni-L] (K_{eq}), slow assembly of the catalytically active species (k_T, k_T^{-1}), an apparent first-order activation step from [R] to [I] (k_a), an irreversible deactivation step [D] (k_d), and the closing of the catalytic cycle via a dark step that produces H$_2$ (k_{HER}). If in such a system k_T and k_T^{-1} are significantly slower compared to the rest of the steps, the *on−off* behavior can be explained, because in the absence of light the dark equilibrium is slow and the amount of [R] and [I] will not change significantly over time. Furthermore, the absence of HER in the dark during the light *on−off* cycles observed in Figure 4b suggests that a k_{HER}-limited homogeneous cycle is unlikely. Then, once nickel enters the cycle as [R] more rapidly due to a light-shifted equilibrium, [R] will build up until the rate of [D] leaving the system irreversibly is equal to the rate of formation of [R], [I] being stationary. This will lead to an expression for activation

of the photocatalytic system such that the activation curve is an exponential asymptote with time constant t_a, which is dominated by electron-transfer rate k_a, a linear deactivation with an apparent time constant t_d, an HER apparent kinetic constant $R_{H_2,max}$, and the apparent transient time t_0 only which corresponds to the initial time delay necessary for the intermediate [I] to be pseudo-stationary (Supporting Information eq S6.2). Our model further provides an accurate fit to the data obtained in both H_2O and D_2O, in line with an expected trend of a KIE. In this case, $R_{H_2,max}$, t_d, and t_0 changed as expected, but the time constant for the activation step (t_a) being independent of the isotopic mass is almost unchanged (Table S2), further corroborating our proposed rate-limiting steps (RLS). Our reaction model not only explains these qualitative trends but also provides an accurate fit with standard errors below 5% for different data sets. It is important to note that acquiring detailed insights into the H_2/D_2 evolution reaction mechanism for the **TpDTz** COF-NiME photocatalytic system became possible only with the use of a flow reactor system.

Our reaction modeling results suggest that as long as a slow catalyst activation time is observed, the RLS of the system is seemingly the electron transfer from the COF to the NiME complex. While this outcome is fully consistent with the assumed outer-sphere electron-transfer process, it reinforces the idea of studying the kinetics of such processes in more detail as this will be crucial to improve the HER rate by rational design of the COF−co-catalyst interface.

CONCLUSIONS

We report the first COF photosensitizer and noble-metal-free molecular co-catalyst photocatalytic system for sustained solar H_2 production from water. This single−site system comprises the newly designed N/S-containing **TpDTz** COF PS that absorbs strongly in the visible region of the solar spectrum and is robust for long-term hydrogen evolution. In combination with an earth-abundant Ni-thiolate cluster co-catalyst which self-assembles in water, we obtain solar H_2 evolution rates as high as 941 μmol h^{-1} g^{-1} and a TON$_{Ni}$ > 103 (70 h) with persistent H_2 evolution for more than 70 h in a single run, which surpasses many benchmark photocatalytic H_2 evolution systems based on COFs and carbon nitrides. To map out the parameter space of this hybrid photocatalytic system, we comprehensively screened the influence of various reaction components, including pH, SED, co-catalyst metal centers, different N/S-containing chelating ligands, and a variety of PSs on the photocatalytic activity. In addition, we have introduced a newly designed continuous-flow system enabling the non-invasive, direct detection of the H_2 production rate. This platform not only provides higher accuracy in quantification; it also paves the way for unprecedented insights into the reaction mechanism which are difficult to obtain with the existing batch measurement methods. Microkinetic modeling of the reaction system suggests that an outer-sphere electron transfer from the photoabsorber to the catalyst is the rate-limiting step, thus spotlighting the importance of the rational design of the COF−co-catalyst interface.

ASSOCIATED CONTENT

Ⓢ Supporting Information

The Supporting Information is available free of charge on the ACS Publications website at DOI: 10.1021/jacs.9b03243.

Synthesis, crystallography, characterizations, and photo-catalysis experimental details, including Figures S1−S58 and Tables S1−S9 (PDF)

AUTHOR INFORMATION

Corresponding Author

*b.lotsch@fkf.mpg.de

ORCID ⓘ

Bishnu P. Biswal: 0000-0002-8565-4550
Tanmay Banerjee: 0000-0002-4548-2117
Gökcen Savasci: 0000-0002-6183-7715
Jürgen Nuss: 0000-0002-0679-0184
Christian Ochsenfeld: 0000-0002-4189-6558
Bettina V. Lotsch: 0000-0002-3094-303X

Notes

The authors declare no competing financial interest.

REFERENCES

(1) (a) Alstrum-Acevedo, J. H.; Brennaman, M. K.; Meyer, T. J. Chemical Approaches to Artificial Photosynthesis. 2. *Inorg. Chem.* **2005**, *44*, 6802−6827. (b) Lewis, N. S.; Nocera, D. G. Powering the Planet: Chemical Challenges in Solar Energy Utilization. *Proc. Natl. Acad. Sci. U. S. A.* **2006**, *103*, 15729−15735. (c) Bard, A. J.; Fox, M. A. Artificial Photosynthesis: Solar Splitting of Water to Hydrogen and Oxygen. *Acc. Chem. Res.* **1995**, *28*, 141−145. (d) U.S. Department of Energy, Energy Information Administration, *Annual Energy Outlook 2013 with Projections to 2040*; U.S. Government Printing Office: Washington, DC, 2013; pp 55−90. (e) Hoffert, M. I.; Caldeira, K.; Jain, A. K.; Haites, E. F.; Harvey, L. D. D.; Potter, S. D.; Schlesinger, M. E.; Schneider, S. H.; Watts, R. G.; Wigley, T. M. L.; Wuebbles, D. J. Energy Implications of Future Stabilization of Atmospheric CO_2 Content. *Nature* **1998**, *395*, 881−884. (f) Vyas, V. S.; Lau, V. W.-h.; Lotsch, B. V. Soft Photocatalysis: Organic Polymers for Solar Fuel Production. *Chem. Mater.* **2016**, *28* (15), 5191−5204.

(2) (a) Banerjee, T.; Gottschling, K.; Savasci, G.; Ochsenfeld, C.; Lotsch, B. V. H_2 Evolution with Covalent Organic Framework Photocatalysts. *ACS Energy Lett.* **2018**, *3* (2), 400−409. (b) Zou, X.; Zhang, Y. Noble Metal-free Hydrogen Evolution Catalysts for Water Splitting. *Chem. Soc. Rev.* **2015**, *44*, 5148−5180.

(3) (a) Cote, A. P.; Benin, A. I.; Ockwig, N. W.; O'Keeffe, M.; Matzger, A. J.; Yaghi, O. M. Porous, Crystalline, Covalent Organic Frameworks. *Science* **2005**, *310* (5751), 1166−70. (b) Feng, X.; Ding, X.; Jiang, D. Covalent Organic Frameworks. *Chem. Soc. Rev.* **2012**, *41* (18), 6010−6022. (c) Xu, S.-Q.; Zhan, T.-G.; Wen, Q.; Pang, Z.-F.; Zhao, X. Diversity of Covalent Organic Frameworks (COFs): A 2D COF Containing Two Kinds of Triangular Micropores of Different Sizes. *ACS Macro Lett.* **2016**, *5* (1), 99−102. (d) Kandambeth, S.;

Dey, K.; Banerjee, R. Covalent Organic Frameworks: Chemistry beyond the Structure. *J. Am. Chem. Soc.* **2019**, *141* (5), 1807−1822.

(4) Keller, N.; Calik, M.; Sharapa, D.; Soni, H. R.; Zehetmaier, P. M.; Rager, S.; Auras, F.; Jakowetz, A. C.; Goerling, A.; Clark, T.; Bein, T. Enforcing Extended Porphyrin J-Aggregate Stacking in Covalent Organic Frameworks. *J. Am. Chem. Soc.* **2018**, *140* (48), 16544−16552.

(5) Feng, X.; Liu, L.; Honsho, Y.; Saeki, A.; Seki, S.; Irle, S.; Dong, Y.; Nagai, A.; Jiang, D. High-rate Charge-carrier Transport in Porphyrin Covalent Organic Frameworks: Switching from Hole to Electron to Ambipolar Conduction. *Angew. Chem., Int. Ed.* **2012**, *51* (11), 2618−2622.

(6) (a) Doonan, C. J.; Tranchemontagne, D. J.; Glover, T. G.; Hunt, J. R.; Yaghi, O. M. Exceptional Ammonia Uptake by a Covalent Organic Framework. *Nat. Chem.* **2010**, *2* (3), 235−238. (b) Oh, H.; Kalidindi, S. B.; Um, Y.; Bureekaew, S.; Schmid, R.; Fischer, R. A.; Hirscher, M. A Cryogenically Flexible Covalent Organic Framework for Efficient Hydrogen Isotope Separation by Quantum Sieving. *Angew. Chem., Int. Ed.* **2013**, *52* (50), 13219−13222. (c) Biswal, B. P.; Chaudhari, H. D.; Banerjee, R.; Kharul, U. K. Chemically Stable Covalent Organic Framework (COF)-Polybenzimidazole Hybrid Membranes: Enhanced Gas Separation through Pore Modulation. *Chem. - Eur. J.* **2016**, *22* (14), 4695−4699. (d) Ji, W.; Xiao, L.; Ling, Y.; Ching, C.; Matsumoto, M.; Bisbey, R. P.; Helbling, D. E.; Dichtel, W. R. Removal of GenX and Perfluorinated Alkyl Substances from Water by Amine-Functionalized Covalent Organic Frameworks. *J. Am. Chem. Soc.* **2018**, *140* (40), 12677−12681. (e) Sun, Q.; Aguila, B.; Earl, L. D.; Abney, C. W.; Wojtas, L.; Thallapally, P. K.; Ma, S. Covalent Organic Frameworks as a Decorating Platform for Utilization and Affinity Enhancement of Chelating Sites for Radionuclide Sequestration. *Adv. Mater.* **2018**, *30* (20), No. 1705479.

(7) (a) Das, G.; Biswal, B. P.; Kandambeth, S.; Venkatesh, V.; Kaur, G.; Addicoat, M.; Heine, T.; Verma, S.; Banerjee, R. Chemical Sensing in Two Dimensional Porous Covalent Organic Nanosheets. *Chem. Sci.* **2015**, *6* (7), 3931−3939. (b) Gao, Q.; Li, X.; Ning, G. H.; Leng, K.; Tian, B.; Liu, C.; Tang, W.; Xu, H. S.; Loh, K. P. Highly Photoluminescent Two-Dimensional Imine-based Covalent Organic Frameworks for Chemical Sensing. *Chem. Commun.* **2018**, *54* (19), 2349−2352.

(8) (a) Keller, N.; Bessinger, D.; Reuter, S.; Calik, M.; Ascherl, L.; Hanusch, F. C.; Auras, F.; Bein, T. Oligothiophene-Bridged Conjugated Covalent Organic Frameworks. *J. Am. Chem. Soc.* **2017**, *139* (24), 8194−8199. (b) Dogru, M.; Bein, T. On the Road towards Electroactive Covalent Organic Frameworks. *Chem. Commun.* **2014**, *50* (42), 5531−46.

(9) Ding, S. Y.; Gao, J.; Wang, Q.; Zhang, Y.; Song, W. G.; Su, C. Y.; Wang, W. Construction of Covalent Organic Framework for Catalysis: Pd/COF-LZU1 in Suzuki−Miyaura Coupling Reaction. *J. Am. Chem. Soc.* **2011**, *133* (49), 19816−19822.

(10) (a) Stegbauer, L.; Schwinghammer, K.; Lotsch, B. V. A Hydrazone-based Covalent Organic Framework for Photocatalytic Hydrogen Production. *Chem. Sci.* **2014**, *5* (7), 2789−2793. (b) Vyas, V. S.; Haase, F.; Stegbauer, L.; Savasci, G.; Podjaski, F.; Ochsenfeld, C.; Lotsch, B. V. A Tunable Azine Covalent Organic Framework Platform for Visible Light-induced Hydrogen Generation. *Nat. Commun.* **2015**, *6*, 8508. (c) Pachfule, P.; Acharjya, A.; Roeser, J.; Langenhahn, T.; Schwarze, M.; Schomaecker, R.; Thomas, A.; Schmidt, J. Diacetylene Functionalized Covalent Organic Framework (COF) for Photocatalytic Hydrogen Generation. *J. Am. Chem. Soc.* **2018**, *140* (4), 1423−1427. (d) Wang, X.; Chen, L.; Chong, S. Y.; Little, M. A.; Wu, Y.; Zhu, W. H.; Clowes, R.; Yan, Y.; Zwijnenburg, M. A.; Sprick, R. S.; Cooper, A. I. Sulfone-containing Covalent Organic Frameworks for Photocatalytic Hydrogen Evolution from Water. *Nat. Chem.* **2018**, *10*, 1180−1189. (e) Banerjee, T.; Lotsch, B. V. The Wetter the Better. *Nat. Chem.* **2018**, *10*, 1175−1177. (f) Haase, F.; Banerjee, T.; Savasci, G.; Ochsenfeld, C.; Lotsch, B. V. Structure-property-activity Relationships in a Pyridine Containing Azine-linked Covalent Organic Framework for Photocatalytic Hydrogen Evolution. *Faraday Discuss.* **2017**, *201*, 247−264.

(11) Barber, J.; Tran, P. D. From Natural to Artificial Photosynthesis. *J. R. Soc., Interface* **2013**, *10* (81), 20120984.

(12) Banerjee, T.; Haase, F.; Savasci, G.; Gottschling, K.; Ochsenfeld, C.; Lotsch, B. V. Single-Site Photocatalytic H$_2$ Evolution from Covalent Organic Frameworks with Molecular Cobaloxime Co-Catalysts. *J. Am. Chem. Soc.* **2017**, *139* (45), 16228−16234.

(13) (a) Zhang, P.; Wang, M.; Dong, J. F.; Li, X. Q.; Wang, F.; Wu, L. Z.; Sun, L. C. Photocatalytic Hydrogen Production from Water by Noble-Metal-Free Molecular Catalyst Systems Containing Rose Bengal and the Cobaloximes of BFx-Bridged Oxime Ligands. *J. Phys. Chem. C* **2010**, *114*, 15868−15874. (b) Fihri, A.; Artero, V.; Razavet, M.; Baffert, C.; Leibl, W.; Fontecave, M. Cobaloxime-based Photocatalytic Devices for Hydrogen Production. *Angew. Chem., Int. Ed.* **2008**, *47*, 564. (c) Du, P. W.; Knowles, K.; Eisenberg, R. A Homogeneous System for the Photogeneration of Hydrogen from Water Based on a Platinum(II) TerpyridylAcetylide Chromophore and a Molecular Cobalt Catalyst. *J. Am. Chem. Soc.* **2008**, *130*, 12576−12577. (d) Lazarides, T.; McCormick, T.; Du, P. W.; Luo, G. G.; Lindley, B.; Eisenberg, R. Making Hydrogen from Water Using a Homogeneous System Without Noble Metals. *J. Am. Chem. Soc.* **2009**, *131*, 9192−9194. (e) Probst, B.; Rodenberg, A.; Guttentag, M.; Hamm, P.; Alberto, R. Highly Stable Rhenium-Cobalt System for Photocatalytic H2 Production: Unraveling the Performance-Limiting Steps. *Inorg. Chem.* **2010**, *49*, 6453−6460.

(14) (a) Hawecker, J.; Lehn, J. M.; Ziessel, R. Efficient Homogenious Photochemical Hydrogen Generation and Water Reduction Mediated by Cobaloxime or Macrocyclic Cobalt Complexes. *Nouv. J. Chim.* **1983**, *7*, 271. (b) McCormick, T. M.; Han, Z. J.; Weinberg, D. J.; Brennessel, W. W.; Holland, P. L.; Eisenberg, R. Impact of Ligand Exchange in Hydrogen Production from Cobaloxime-Containing Photocatalytic Systems. *Inorg. Chem.* **2011**, *50*, 10660−10666.

(15) (a) Han, Z.; McNamara, W. R.; Eum, M. S.; Holland, P. L.; Eisenberg, R. A Nickel Thiolate Catalyst for the Long-lived Photocatalytic Production of Hydrogen in a Noble-metal-free System. *Angew. Chem., Int. Ed.* **2012**, *51* (7), 1667−70. (b) Rao, H.; Yu, W.-Q.; Zheng, H.-Q.; Bonin, J.; Fan, Y.-T.; Hou, H.-W. Highly Efficient Photocatalytic Hydrogen Evolution from Nickel Quinolinethiolate Complexes under Visible Light Irradiation. *J. Power Sources* **2016**, *324*, 253−260. (c) Das, A.; Han, Z.; Brennessel, W. W.; Holland, P. L.; Eisenberg, R. Nickel Complexes for Robust Light-Driven and Electrocatalytic Hydrogen Production from Water. *ACS Catal.* **2015**, *5* (3), 1397−1406.

(16) (a) Bouwman, E.; Reedijk, J. Structural and Functional Models related to the Nickel Hydrogenases. *Coord. Chem. Rev.* **2005**, *249*, 1555−1581. (b) Fontecilla-Camps, J. C.; Volbeda, A.; Cavazza, C.; Nicolet, Y. Structure/Function Relationships of [NiFe]- and [FeFe]-Hydrogenases. *Chem. Rev.* **2007**, *107*, 4273−4303. (c) Tard, C.; Pickett, C. J. Structural and Functional Analogues of the Active Sites of the [Fe]-, [NiFe]-, and [FeFe]-Hydrogenases. *Chem. Rev.* **2009**, *109*, 2245−2274. (d) Carroll, M. E.; Barton, B. E.; Gray, D. L.; Mack, A. E.; Rauchfuss, T. B. Active-Site Models for the Nickel−Iron Hydrogenases: Effects of Ligands on Reactivity and Catalytic Properties. *Inorg. Chem.* **2011**, *50*, 9554−9563.

(17) (a) Bevk, D.; Marin, L.; Lutsen, L.; Vanderzande, D.; Maes, W. Thiazolo[5,4-d]thiazoles − Promising Building Blocks in the Synthesis of Semiconductors for Plastic Electronics. *RSC Adv.* **2013**, *3* (29), 11418. (b) Dessì, A.; Calamante, M.; Mordini, A.; Peruzzini, M.; Sinicropi, A.; Basosi, R.; Fabrizi de Biani, F.; Taddei, M.; Colonna, D.; di Carlo, A.; Reginato, G.; Zani, L. Thiazolo[5,4-d]thiazole-based Organic Sensitizers with Strong Visible Light Absorption for Transparent, Efficient and Stable Dye-sensitized Solar Cells. *RSC Adv.* **2015**, *5* (41), 32657−32668. (c) Olgun, U.; Gülfen, M. Effects of Different Dopants on the Band Gap and Electrical Conductivity of the Poly(phenylene-thiazolo[5,4-d]-thiazole) Copolymer. *RSC Adv.* **2014**, *4* (48), 25165−25171. (d) Woodward, A. N.; Kolesar, J. M.; Hall, S. R.; Saleh, N. A.; Jones, D. S.; Walter, M. G. Thiazolothiazole Fluorophores Exhibiting

Strong Fluorescence and Viologen-Like Reversible Electrochromism. *J. Am. Chem. Soc.* **2017**, *139* (25), 8467−8473.

(18) Zhang, W.; Hong, J.; Zheng, J.; Huang, Z.; Zhou, J. S.; Xu, R. Nickel−Thiolate Complex Catalyst Assembled in One Step in Water for Solar H$_2$ Production. *J. Am. Chem. Soc.* **2011**, *133*, 20680−20683.

(19) Zhu, Y.; Zhang, W. Reversible Tuning of Pore Size and CO2 Adsorption in Azobenzene Functionalized Porous Organic Polymers. *Chem. Sci.* **2014**, *5*, 4957−4961.

(20) (a) Kussmann, J.; Ochsenfeld, C. Pre-selective screening for matrix elements in linear-scaling exact exchange calculations. *J. Chem. Phys.* **2013**, *138*, 134114. (b) Kussmann, J.; Ochsenfeld, C. Preselective screening for linear-scaling exact exchange-gradient calculations for graphics processing units and general strong-scaling massively parallel calculations. *J. Chem. Theory Comput.* **2015**, *11*, 918−922. (c) Ahlrichs, R.; Bär, M.; Häser, M.; Horn, H.; Kölmel, C. Electronic structure calculations on workstation computers: The program system turbomole. *Chem. Phys. Lett.* **1989**, *162*, 165−169. (d) TURBOMOLE V7.3, 2018; A development of University of Karlsruhe and Forschungszentrum Karlsruhe GmbH, 1989−2007; TURBOMOLE GmbH, since 2007; available from http://www.turbomole.com.

(21) Kandambeth, S.; Mallick, A.; Lukose, B.; Mane, M. V.; Heine, T.; Banerjee, R. Construction of Crystalline 2D Covalent Organic Frameworks with Remarkable Chemical (Acid/Base) Stability via a Combined Reversible and Irreversible Route. *J. Am. Chem. Soc.* **2012**, *134* (48), 19524−19527.

(22) (a) Peng, L.-Z.; Liu, P.; Cheng, Q.-Q.; Hu, W.-J.; Liu, Y. A.; Li, J.-S.; Jiang, B.; Jia, X.-S.; Yang, H.; Wen, K. Highly Effective Electrosynthesis of Hydrogen Peroxide from Oxygen on a Redox-active Cationic Covalent Triazine Network. *Chem. Commun.* **2018**, *54*, 4433−4436. (b) Wei, P.-F.; Qi, M.-Z.; Wang, Z.-P.; Ding, S.-Y.; Yu, W.; Liu, Q.; Wang, L.-K.; Wang, H.-Z.; An, W.-K.; Wang, W. Benzoxazole-Linked Ultrastable Covalent Organic Frameworks for Photocatalysis. *J. Am. Chem. Soc.* **2018**, *140*, 4623−4631.

(23) (a) Cardona, C. M.; Li, W.; Kaifer, A. E.; Stockdale, D.; Bazan, G. C. Electrochemical Considerations for Determining Absolute Frontier Orbital Energy Levels of Conjugated Polymers for Solar Cell Applications. *Adv. Mater.* **2011**, *23*, 2367−2371. (b) Calik, M.; Auras, F.; Salonen, L. M.; Bader, K.; Grill, I.; Handloser, M.; Medina, D. D.; Dogru, M.; Löbermann, F.; Trauner, D.; Hartschuh, A.; Bein, T. Extraction of Photogenerated Electrons and Holes from a Covalent Organic Framework Integrated Heterojunction. *J. Am. Chem. Soc.* **2014**, *136*, 17802−17807. (c) Zhao, W.; Zhuang, X.; Wu, D.; Zhang, F.; Gehrig, D.; Laquai, F.; Feng, X. Boron-π-nitrogen-based Conjugated Porous Polymers with Multi-functions. *J. Mater. Chem. A* **2013**, *1*, 13878−13884. (d) Pellegrin, Y.; Odobel, F. , Sacrificial electron donor reagents for solar fuel production. *C. R. Chim.* **2017**, *20* (3), 283−295.

(24) (a) Kagalwala, H. N.; Gottlieb, E.; Li, G.; Li, T.; Jin, R.; Bernhard, S. Photocatalytic Hydrogen Generation System Using a Nickel-Thiolate Hexameric Cluster. *Inorg. Chem.* **2013**, *52*, 9094−9101. (b) Gould, R. O.; Harding, M. M. Nickel and Palladium Complexes of 1-Hydroxyethane-2-thiol and Analogues. Part 1. Crystal Structure of Cydohexakis[bis-(p-I -hydroxyethane-2-thiolato) -nickel (II)]. *J. Chem. Soc. A* **1970**, *0*, 875−881.

(25) (a) Schwinghammer, K.; Tuffy, B.; Mesch, M. B.; Wirnhier, E.; Martineau, C.; Taulelle, F.; Schnick, W.; Senker, J.; Lotsch, B. V. Triazine-based Carbon Nitrides for Visible-Light-Driven Hydrogen Evolution. *Angew. Chem., Int. Ed.* **2013**, *52*, 2435−2439. (b) Zhang, J.; Chen, X.; Takanabe, K.; Maeda, K.; Domen, K.; Epping, J. D.; Fu, X.; Antonietti, M.; Wang, X. Synthesis of a Carbon Nitride Structure for Visible-light Catalysis by Copolymerization. *Angew. Chem., Int. Ed.* **2010**, *49*, 441−444. (c) Indra, A.; Menezes, P. W.; Kailasam, K.; Hollmann, D.; Schroder, M.; Thomas, A.; Bruckner, A.; Driess, M. Nickel as a Co-catalyst for Photocatalytic Hydrogen Evolution on Graphitic-carbon Nitride (sg-CN): What is the nature of the Active Species? *Chem. Commun.* **2016**, *52*, 104−107. (d) Kasap, H.; Caputo, C. A.; Martindale, B. C.; Godin, R.; Lau, V. W.; Lotsch, B. V.; Durrant, J. R.; Reisner, E. Solar-Driven Reduction of Aqueous Protons Coupled to Selective Alcohol Oxidation with a Carbon Nitride−Molecular Ni Catalyst System. *J. Am. Chem. Soc.* **2016**, *138* (29), 9183−9192. (e) Zeng, D.; Ong, W.-J.; Zheng, H.; Wu, M.; Chen, Y.; Peng, D.-L.; Han, M.-Y. Ni$_{12}$P$_5$ Nanoparticles Embedded into Porous g-C$_3$N$_4$Nanosheets as a Noble-metal-free Hetero-structure Photocatalyst for Efficient H2 Production under Visible Light. *J. Mater. Chem. A* **2017**, *5*, 16171−16178. (f) Martindale, B. C. M.; Hutton, G. A. M.; Caputo, C. A.; Reisner, E. Solar Hydrogen Production Using Carbon Quantum Dots and a Molecular Nickel Catalyst. *J. Am. Chem. Soc.* **2015**, *137*, 6018−6025.

(26) Nanda, J.; Sapra, S.; Sarma, D. D.; Chandrasekharan, N.; Hodes, G. Size-Selected Zinc Sulfide Nanocrystallites: Synthesis, Structure, and Optical Studies. *Chem. Mater.* **2000**, *12*, 1018−1024.

(27) Biswal, B. P.; Becker, D.; Chandrasekhar, N.; Seenath, J. S.; Paasch, S.; Machill, S.; Hennersdorf, F.; Brunner, E.; Weigand, J. J.; Berger, R.; Feng, X. Exploration of Thiazolo[5,4-d]thiazole Linkages in Conjugated Porous Organic Polymers for Chemoselective Molecular Sieving. *Chem. - Eur. J.* **2018**, *24* (42), 10868−10875.